

A Facile Synthesis of α -Fe₂O₃/Carbon Nanotubes and Their Photocatalytic and Electrochemical Sensing Performances

Adel A. Ismail^{1,*}, Atif Mossad Ali^{2,3,**}, Farid A. Harraz^{1,4}, M. Faisal⁴, H. Shoukry²,
A.E. Al-Salami²

¹ Nanomaterials and Nanotechnology Department, Central Metallurgical Research and Development Institute (CMRDI), P.O. 87 Helwan, Cairo 11421, Egypt

² Department of Physics, Faculty of Science, King Khalid University, Abha, Saudi Arabia

³ Department of Physics, Faculty of Science, Assiut University, Assiut, Egypt

⁴ Promising Centre for Sensors and Electronic Devices, Advanced Materials and Nano-Research Centre, Najran University, Najran, Saudi Arabia.

*E. mail: adelali141@yahoo.com, atifali@kku.edu.sa

Received: 5 October 2018 / Accepted: 31 October 2018 / Published: 30 November 2018

This study reports a simple process for synthesizing efficient photocatalyst based on mesoporous carbon nanotubes (CNT)- α -Fe₂O₃ nanohybrids at different CNT contents as well as their photocatalytic performance under visible light illumination. TEM image of CNT- α -Fe₂O₃ nanohybrid exhibited that Fe₂O₃ nanoparticles are well distributed homogeneously in the CNT surface with size of <10 nm and lattice fringes were obviously assigned with a spacing of 0.252 nm, conforming to the (110) planes of α -Fe₂O₃. The prepared mesoporous CNT- α -Fe₂O₃ nanohybrids act as efficient and reusable photocatalysts for the photocatalytic oxidation of Bismarck Brown R (BBR) Dye. The total removal efficiency was boosted from 83 to 98% with the increase of CNT contents from 0 to 50%. The decolorization rate of BBR dye over 50% CNT- α -Fe₂O₃ nanohybrid is greater by almost 35 times than that of the pure mesoporous Fe₂O₃. The superior photocatalytic performance of mesoporous CNT- α -Fe₂O₃ nanohybrids over mesoporous α -Fe₂O₃ is mainly owing to the synergistic effect and effective retard electron-hole recombination at the CNT/Fe₂O₃ interfaces. The high photocatalytic performance and easily recyclable of CNT- α -Fe₂O₃ nanohybrids come to be promising photocatalyst and adsorbent for industrial and domestic wastewater treatment. Furthermore, the optimal sample of 50% CNT- α -Fe₂O₃ modified glassy carbon electrode (GCE) was examined to the electrochemical detection and determination of phenyl-hydrazine. The sensor electrode exhibited outstanding sensitivity of 1081 $\mu\text{AmM}^{-1}\text{cm}^{-2}$ within a linear dynamic range from 10 μM to 1 mM with a correlation coefficient $R^2 = 0.9995$ and a low limit of detection (LOD) 6.25 μM .

Keywords: CNT- α -Fe₂O₃; Nanohybrids; Electrochemical sensing; Photocatalyst; Photodegradation

1. INTRODUCTION

Synthesis of novel photocatalysts with high reliability, sensitivity, and excellent absorptivity/removal efficiency has paid great attention for the last two decades, driven by their broad applications for the wastewater treatment, air purification and hydrogen production [1]. Carbon nanotubes (CNTs) are considered to be intelligent supports for photocatalysts owing to their chemical stability, large surface area and high electron conductivity [2]. In order to get the optimization for employing of nanotubes in different applications, it is indispensable to connect nanostructure materials or functional groups onto their surface. Up till now, several metals, for example, nickel (Ni), copper (Cu) [3], platinum (Pt) [4], iron (Fe) and cobalt (Co) [5], and oxide particles such as silicon dioxide (SiO₂) [6], tin dioxide (SnO₂) [7], aluminium oxide (Al₂O₃) [8] and titanium dioxide (TiO₂) [9], were deposited onto carbon nanotubes surface. For example, the combination of TiO₂ with activated carbon led to promote the photocatalytic performance under visible light illumination [10]. A combined effect between semiconductors and CNT is expected to produce promising materials for photocatalysis application due to its high charge transfer approaches across the semiconductors and CNT interface. In recently published papers, CNT-SnO₂ hybrids revealed high sensitivity in gas sensors [11], CNT-zinc oxide (ZnO) has improved the photovoltaic efficiencies [12] and CNT-manganese dioxide (MnO₂), ruthenium oxide (RuO₂) nanocomposites have enhanced the supercapacitor capacities [13,14]. On the other hand, iron oxides are employed in different applications such as catalysis, magnetic storage, sensors and rechargeable lithium batteries especially in nanoscale sizes [15-17]. Three-dimensional (3D) porous CNT/MnO₂ composite electrode synthesized by a facile process "dipping and drying" followed by a potentiostatic deposition technique for supercapacitor applications and non-enzymatic glucose detection has been reported [18]. The 3D porous CNT/MnO₂ composite paved the way for this nanohybrid to be a likely competitive material in the supercapacitor and glucose sensor application. Among all iron oxides available, hematite (α -Fe₂O₃) is very stable under ambient conditions with the superiority of high resistance to corrosion and less expensive. Mesoporous α -Fe₂O₃ with mesoporous structures using soft and hard template methods have been synthesized [19-21]. Mesoporous semiconductors candidates have received considerable interest for their potential applications such as sensors, gas separators, photo-/catalysts, and energy converters [22-25]. In a previous work [26], α -Fe₂O₃ nanoparticles were prepared by hydrothermal technique. As-prepared α -Fe₂O₃ nanoparticles were used as efficient electrons for the production of efficient and strong chemical sensor for the effective and highly sensitive detection of phenyl-hydrazine. In the present work, a facile synthesis to fabricate highly photoactive mesoporous CNT- α -Fe₂O₃ nanohybrids at different CNT contents has been demonstrated. The main goal of this contribution is evaluating the significance of the mesoporous CNT/ α -Fe₂O₃ interface by optimizing the hybrids' interfacial area and fully comparing their photocatalytic activity under visible light illumination. Additionally, to examine the electrochemical sensing performance of as-formed nanohybrid coated onto glassy carbon electrode for the determination and sensing of phenyl-hydrazine in aqueous solutions using the current-potential (*I-V*) technique. The optimized mesoporous 50%CNT- α -Fe₂O₃ nanohybrid indicated the highest photocatalytic efficiency compared with mesoporous α -Fe₂O₃. The photocatalytic performance of mesoporous CNT- α -Fe₂O₃ nanohybrids for photocatalytic oxidation of BBR dye indicates that this nanohybrid is a favorable candidate as

photocatalyst and absorbent for industrial and domestic wastewater treatment as well as effective electrochemical sensor electrode.

2. EXPERIMENTAL DETAIL

Iron (III) acetylacetonate (97%, $\text{Fe}(\text{C}_5\text{H}_7\text{O}_2)_3$), Multiwall Carbon Nanotubes (MWCNT), the block copolymer surfactant $\text{EO}_{106}\text{-PO}_{70}\text{EO}_{106}$ (F-127, $\text{EO} = -\text{CH}_2\text{CH}_2\text{O}-$, $\text{PO} = -\text{CH}_2(\text{CH}_3)\text{CHO}-$, MW 12600 g/mol), Bismarck Brown R (BBR) Dye, CH_3COOH , $\text{C}_2\text{H}_5\text{OH}$, and HCl were purchased from Sigma-Aldrich.

Mesoporous $\text{CNT-}\alpha\text{-Fe}_2\text{O}_3$ nanohybrids are synthesized using the sol-gel approach by adding F127 triblock copolymer as a template agent. To uniformly disperse mesoporous $\alpha\text{-Fe}_2\text{O}_3$ nanoparticles into the Multiwall Carbon Nanotubes (MWCNT), we exploit a multi-component assembly process, wherein the F127, Fe_2O_3 , and MWCNT are assembled in a single-step process. In a typical procedure, 2.4 g of F127 is added to 30 mL ethanol through magnetic stirring and then 0.74 mL of HCl , 2.3 mL of CH_3COOH and 2.28 g of $\text{Fe}(\text{C}_5\text{H}_7\text{O}_2)_3$ are put together to dissolved surfactant to obtain mesophase. The solution is maintained with string for 60 min. Finally, MWCNT is gradually added to the above mesophase to obtain $\alpha\text{-Fe}_2\text{O}_3\text{-CNT}$ nanohybrids with vigorously stirring for 2 hours. For drying the obtained sol, the mixture is transferred into a Petri dish in drier at 40 °C with 40-80% humidity for 12 h, then the temperature of drier raised to 65 °C for 24 h. The as-prepared hybrids are annealed at 500 °C for 4 h with very slow a heating rate and a cooling rate of 1 °C /min and 2 °C/min, respectively to get mesoporous $\text{CNT-}\alpha\text{-Fe}_2\text{O}_3$ nanohybrids at different CNT contents 10, 20, 40 and 50 wt%.

There will be a detailed physicochemical characterization of the developed mesoporous $\text{CNT-}\alpha\text{-Fe}_2\text{O}_3$ nanohybrids to have better understanding of their structure, surface morphology, and composition. a JEOL JEM-2100F-UHR field-emission instrument equipped with a Gatan GIF 2001 energy filter and a 1k-CCD camera was used at 200 kV to obtain TEM images and EEL spectra. FE scanning electron microanalyzer (JEOL-6300F, 5 kV) was employed to determine SEM images. A Quantachrome Autosorb 3B was used to determine the nitrogen adsorption-desorption isotherms at 77 K after outgassing at 200 °C. The sorption data were determined to employ Halsey equation by Barrett-Joyner-Halenda (BJH) model. Bruker AXS D4 Endeavour X diffractometer was employed to determine the X-ray diffraction data using $\text{Cu K}\alpha_{1/2}$, $\lambda_{\alpha_1} = 154.060$ pm, $\lambda_{\alpha_2} = 154.439$ pm radiation. Bruker Optics IFS66v/s FTIR spectrometer with FRA-106 Raman attachment was used to record Raman spectra. BRUKER FRA 106 spectrometer was used to measure FT-IR spectra employing the standard KBr pellet method. Diffuse reflectance spectroscopy (DRS) was measured by Varian Cary 100 Scan UV-vis system equipped with a Labsphere integrating sphere to determine the reflectance spectra of the prepared photocatalysts over a range of 200-800 nm. The bandgap energy of the prepared photocatalysts was calculated using DRS.

A glassy carbon electrode (GCE) with a surface area 0.071 cm^2 was used as the working electrode after modification with the active material (50% $\text{CNT-}\alpha\text{-Fe}_2\text{O}_3$ nanohybrid). The synthesized material was mixed smoothly with the appropriate amount of a conducting binder from both ethyl acetate and butyl carbitol acetate to achieve a mixed past. The coated GCE was dried in an oven at 65 °C for 6 h. Zahner - Zennium, Germany, electrochemical workstation was used to connect the electrochemical cell with a two - electrodes system; the $\text{CNT-}\alpha\text{-Fe}_2\text{O}_3$ modified GCE served as a working electrode, whereas

a Pt wire acted as a counter electrode. A 0.1M of phosphate buffer solution (PBS) with a pH=7.0 was used as an electrolyte. The sensing and quantification of phenyl-hydrazine with different concentrations ranging from 10 μ M up to 10 mM were performed via measuring the current-potential (*I-V*) characteristics within the potential window 0.0 to 1.5 V. The electrochemical measurements were conducted without stirring, at room temperature. The sensor sensitivity was estimated from the slope of the calibration plot divided by the electrode surface area.

The synthesized mesoporous Fe₂O₃ nanoparticles and CNT- α -Fe₂O₃ nanohybrids were evaluated to determine their photocatalytic activity by photodegradation of Bismarck Brown R (BBR) dye as a pollutant model under visible light illumination. The systematic experiments were performed in a 100 ml photoreactor maintained - a magnetic stirrer and 250 W lamps (Osram, Germany) as visible light irradiation source horizontally fixed overhead the photoreactor. In the dark, 0.5 g/l of the prepared photocatalysts was added to 100 ml of BBR [5×10^{-5} M] as a pollutant model with magnetically stirring for 60 min to reach adsorption equilibrium. The adsorption amount of BBR over the CNT- α -Fe₂O₃ nanohybrids could be determined. In an illumination test, the air is pumped to the photocatalysis reaction to provide molecular oxygen and enhance the photoreaction mechanism. At regular intervals, the suspended solution was withdrawn and the solid was separated by centrifuge to analyze the filtrate. The decolorization BBR dye was recorded by Varian Cary 100 Scan UV-vis system to determine its absorbance at 468 nm conforming to the maximum wavelength of BBR at interval time. The change in absorption intensity of the irradiated solution after centrifugation was carried out using UV-VIS spectrophotometer. To check the mineralization of BBR dye, Phoenix 8000 UV-persulfate TOC Analyzer was employed to measure the total organic carbon (TOC).

3. RESULTS AND DISCUSSION

3.1. Structural Investigations

The XRD technique is employed to determine the crystalline construction of the mesoporous CNT-Fe₂O₃ nanohybrids at different CNT contents 10, 20, 40 and 50 wt%. Fig. 1 shows the XRD patterns for the mesoporous CNT-Fe₂O₃ nanohybrids as compared with the pure Fe₂O₃ nanoparticles. The peaks of the as-prepared Fe₂O₃ observed at $2\theta = 24.16^\circ$, 40.84° , 54.02° , 57.54° and 62.44° assigned for the (012), (113), (116), (018) and (214) planes, respectively, are in agreement with the theoretical data (hematite, JCPDS, file no. 33-0664), evidencing the presence of α -Fe₂O₃ with a suitable crystallinity to rhombohedral corundum structure along with one impure peak corresponding to (400) plane of γ -Fe₂O₃ (maghemite, JCPDS, file no. 39-1346). Moreover, the (002) plane characteristic peak of MWCNT at $2\theta = 28.38^\circ$ has been observed for the composite with the highest MWCNT ratio (50% MWCNT/Fe₂O₃). Nevertheless, it was very low, it emphasizes that the prepared nanohybrids comprise MWCNT. The intensities of the characteristic peaks of graphite carbon are approximately declined because CNTs were covered by Fe₂O₃ catalysts. In contrast to the graphite at $2\theta = 26.5^\circ$, this peak exhibits an upward shift, which is explained by a decrease in the sp², C=C layers spacing [27].

In order to further identify the CNT- α -Fe₂O₃ nanohybrids, the Raman spectral analysis was performed. The Raman spectra are shown in Fig.2. These spectra exhibit many peaks at 315, 382, 540, 718, 851, 1036, 1143, 1316, 1668, 1951, 2200, 2420, 2600, 2865 and 3000 cm⁻¹. There are seven Raman-active vibration modes for Fe₂O₃ [28,29], two A_{1g} modes located at 223 cm⁻¹ and 498 cm⁻¹, respectively. Five E_g modes located at 256 cm⁻¹, 292 cm⁻¹, 299 cm⁻¹, 408 cm⁻¹ and 607 cm⁻¹, respectively, in good agreement with the present work. For carbon structure, the Raman spectra contain three bands at 1306 cm⁻¹ (D band), 1596 cm⁻¹ (G band), and 2604 cm⁻¹ (G' band) which are explained by the A_{1g} stretching mode of disordered graphitic structure, E_{2g} C–C stretching mode of an ordered graphitic structure and highly defective MWCNT structure, respectively [3].

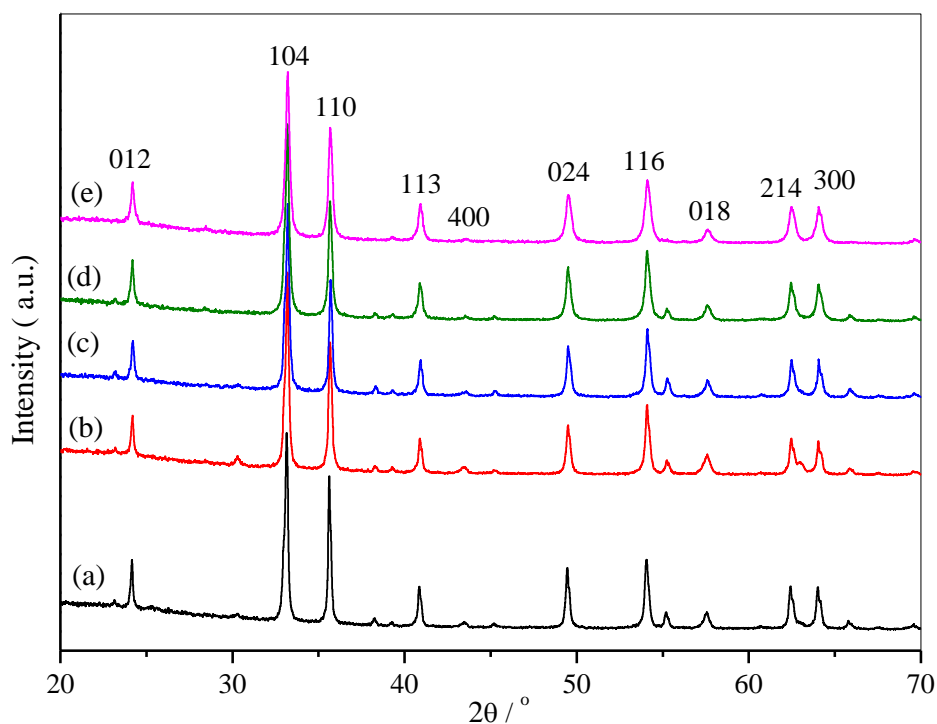


Figure 1. XRD patterns for the mesoporous Fe₂O₃ (a) and CNT-Fe₂O₃ nanohybrids at different CNT content 10 wt% (b), 20 wt% (c), 40 wt% (d) and 50 wt% (e).

Furthermore, there is a mean peak at about 1311 cm⁻¹, it is attributed to the D mode of MWCNTs [30]. α -Fe₂O₃ nanoplates synthesized by a facile alcohol-thermal reaction [28]. Raman spectra show eight Raman peaks at 223, 498, 242, 287, 412, 608, 1310, and 1415 cm⁻¹. The first two peaks are related to A_{1g} mode, from the third peak to the sixth peak are assigned to E_g mode, and the last two peaks may be attributed to 2LO line and vibration of carboxylate group, respectively. In addition, the following bands are observed for MWCNTs prepared by a chemical vapor deposition: D-band at 1270 cm⁻¹ (assigned to the disordered and defect sites of MWCNTs), G-band at 1592 cm⁻¹ (related to the tangential vibration of the C atoms), the defect-induced M-band at 1740 cm⁻¹, G'-band at 2540 cm⁻¹, the band at 1070 cm⁻¹ owing to the existence of amorphous carbon, and the intense peak at 303 cm⁻¹, respectively [29]. Most of these peaks in [28,29] correspond well to the reported values of the present work.

The FT-IR spectra of the mesoporous Fe_2O_3 and CNT- α - Fe_2O_3 nanohybrids are depicted in Fig. 3 in the range of 400 - 4000 cm^{-1} . As could be seen; there are distinguished absorption bands at 3430 and 1650 cm^{-1} corresponding to OH stretching.

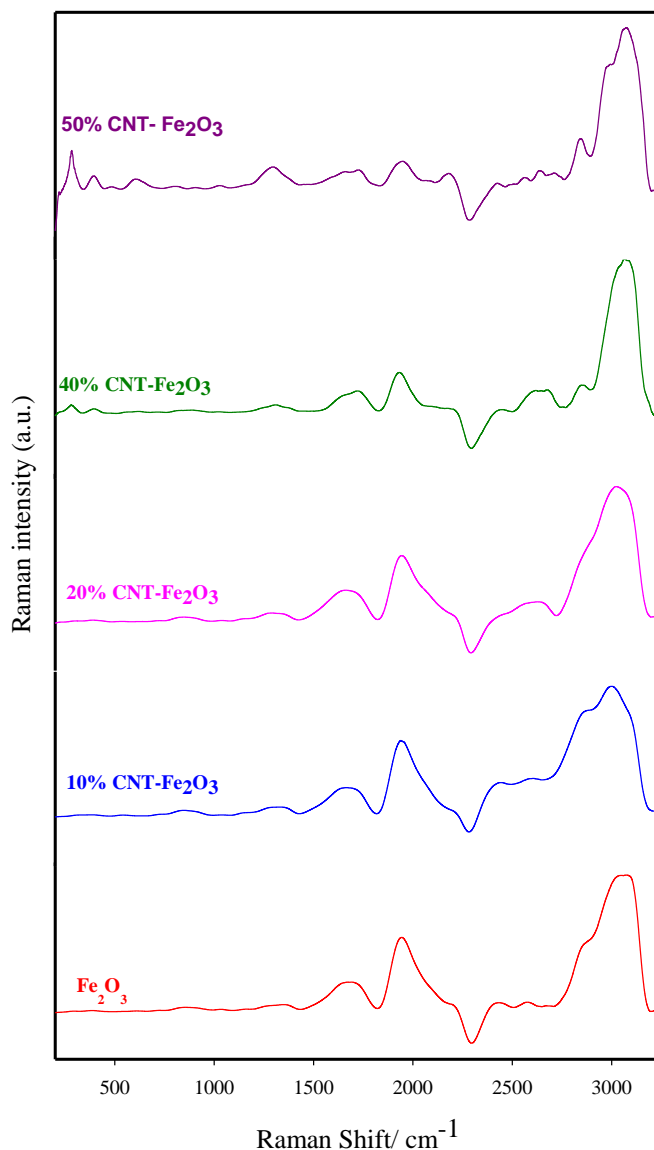


Figure 2. Raman spectra for the mesoporous Fe_2O_3 and CNT- Fe_2O_3 nanohybrids at different CNT contents 10, 20, 40 and 50 wt%.

These peaks can be determined to the alcohol, hydroxylic group, or carboxylic group ($\text{O}=\text{C}-\text{OH}$) [31]. While an absorbance band at 555 cm^{-1} is assigned to the absorbance associated with the characteristic Fe-O stretching modes of α - Fe_2O_3 , it gives further evidence on the formation of α - Fe_2O_3 phase [32]. This peak became slightly stronger with the loading of CNTs, which may correspond to a partial vacancy ordering in the octahedral positions in α - Fe_2O_3 inverse spinel crystal structure [33]. The CNT- α - Fe_2O_3 nanohybrids exhibited an additional band at 2938 cm^{-1} which is assigned as the stretching vibration of C-H bonds [34].

The N₂ adsorption-desorption isotherm of the mesoporous CNT- α -Fe₂O₃ nanohybrids is depicted in Fig. 4. This isotherm could be addressed as IV isotherm type with a typical H3 hysteresis loop distinguished the mesoporous structure material [35]. The adsorption amount was gradually increased for all the developed mesoporous CNT- α -Fe₂O₃ nanohybrids - at a relative pressure of P/P₀ = 0.01-1. The surface area and the pore volume of mesoporous Fe₂O₃ increased from 3.18 m²g⁻¹ to 9.24 m²g⁻¹ and 0.009 and 0.029 cm³ g⁻¹ with the increase of CNT content from 0 to 50%, respectively. The surface area values, total pore volumes and average pore diameters for all prepared photocatalysts are determined and listed in Table 1.

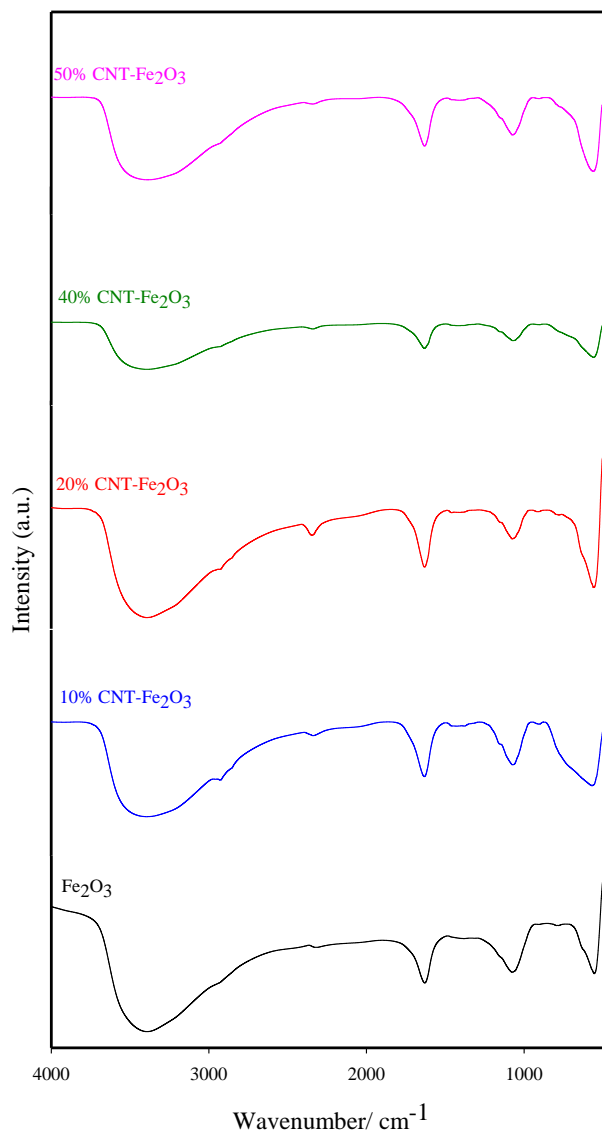


Figure 3. FT-IR spectra for the mesoporous Fe₂O₃ and CNT-Fe₂O₃ nanohybrids at different CNT contents 10, 20, 40 and 50 wt%.

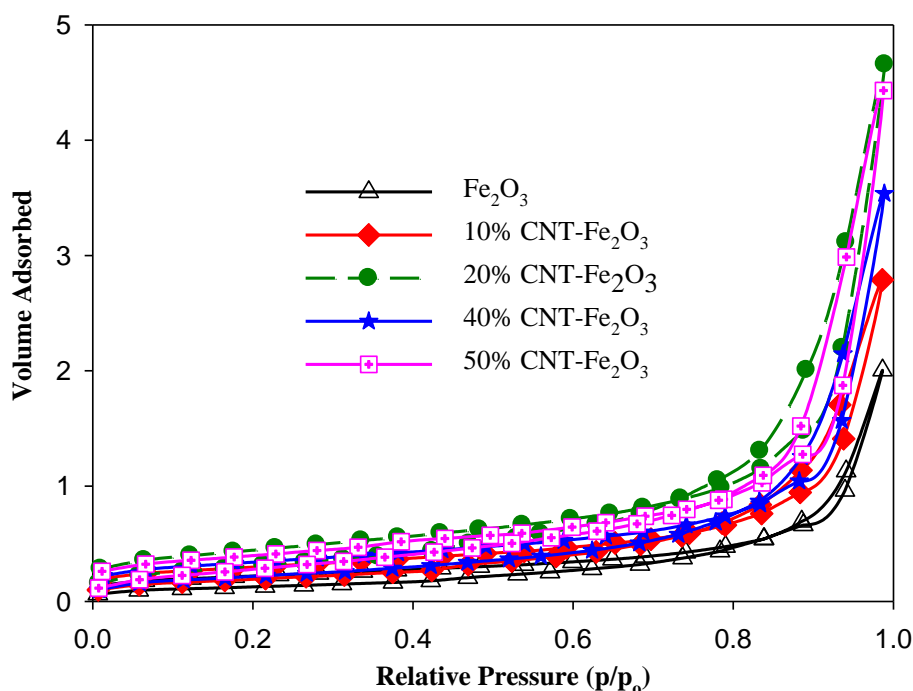


Figure 4. N₂ sorption isotherms of mesoporous Fe₂O₃ and CNT-Fe₂O₃ nano hybrids at 10 and 50 wt% CNT contents.

Table 1. Textural properties of mesoporous α -Fe₂O₃ and CNT- α -Fe₂O₃ nano hybrids at different CNT contents and their photocatalytic properties.

Photo-catalysts	S_{BET}/m^2g^{-1}	V_p (cm ³ /g)	D_p (nm)	Adsorption efficiency, %	$r, 10^4$ (molL ⁻¹ s ⁻¹)	Decolorization, %	%TOC Removal efficiency
Meso-Fe ₂ O ₃	3.18 ± 0.5	0.009 ± 0.001	16.4 ± 2	5.0 ± 2	0.13 ± 0.01	61 ± 3	83 ± 2
10% CNT	6.36 ± 0.5	0.020 ± 0.001	18.6 ± 2	50 ± 5	2.33 ± 0.02	69 ± 3	87 ± 2
20% CNT	7.02 ± 0.5	0.022 ± 0.001	16.4 ± 2	70 ± 5	3.11 ± 0.1	83 ± 3	91 ± 2
40% CNT	8.46 ± 0.5	0.026 ± 0.001	18.6 ± 2	80 ± 5	4.32 ± 0.1	87 ± 3	95 ± 2
50% CNT	9.24 ± 0.5	0.029 ± 0.001	24.0 ± 2	85 ± 5	4.55 ± 0.1	95 ± 3	98 ± 2

S_{BET} Surface area, V_p pore volume, D_p pore diameter, r decolorization rate

These textural properties and particle size of the mesoporous α -Fe₂O₃ and CNT- α -Fe₂O₃ nano hybrids at different CNT contents were further investigated using FESEM (Fig. 5). It is clearly seen from FESEM images, Fig. 5(a-e), that in contrast to the spherical α -Fe₂O₃ particles (Fig. 5a), the morphology of the CNT- α -Fe₂O₃ nano hybrids is quite different, suggesting that the introduction of CNT at different contents from 10-50 wt% has a considerable effect in tuning the Fe₂O₃ morphology (Fig. 5b-e)).

The FESEM image exhibited that the α -Fe₂O₃ particles are formed tiny spherical with size ~ 20-40 nm, with some aggregation to form large spherical particles with size ~50-100 nm. The energy-dispersive spectrometry spectrum of 50% CNT- α -Fe₂O₃ nano hybrid is displayed in Fig. 5f, confirming

that Fe, Ti, C and O atoms are distributed uniformly in the CNT- α -Fe₂O₃. In general, the presence of α -Fe₂O₃ nanoparticles with uniformly and dispersed onto the CNT surface is playing a vital role for efficient adsorption and photocatalytic applications.

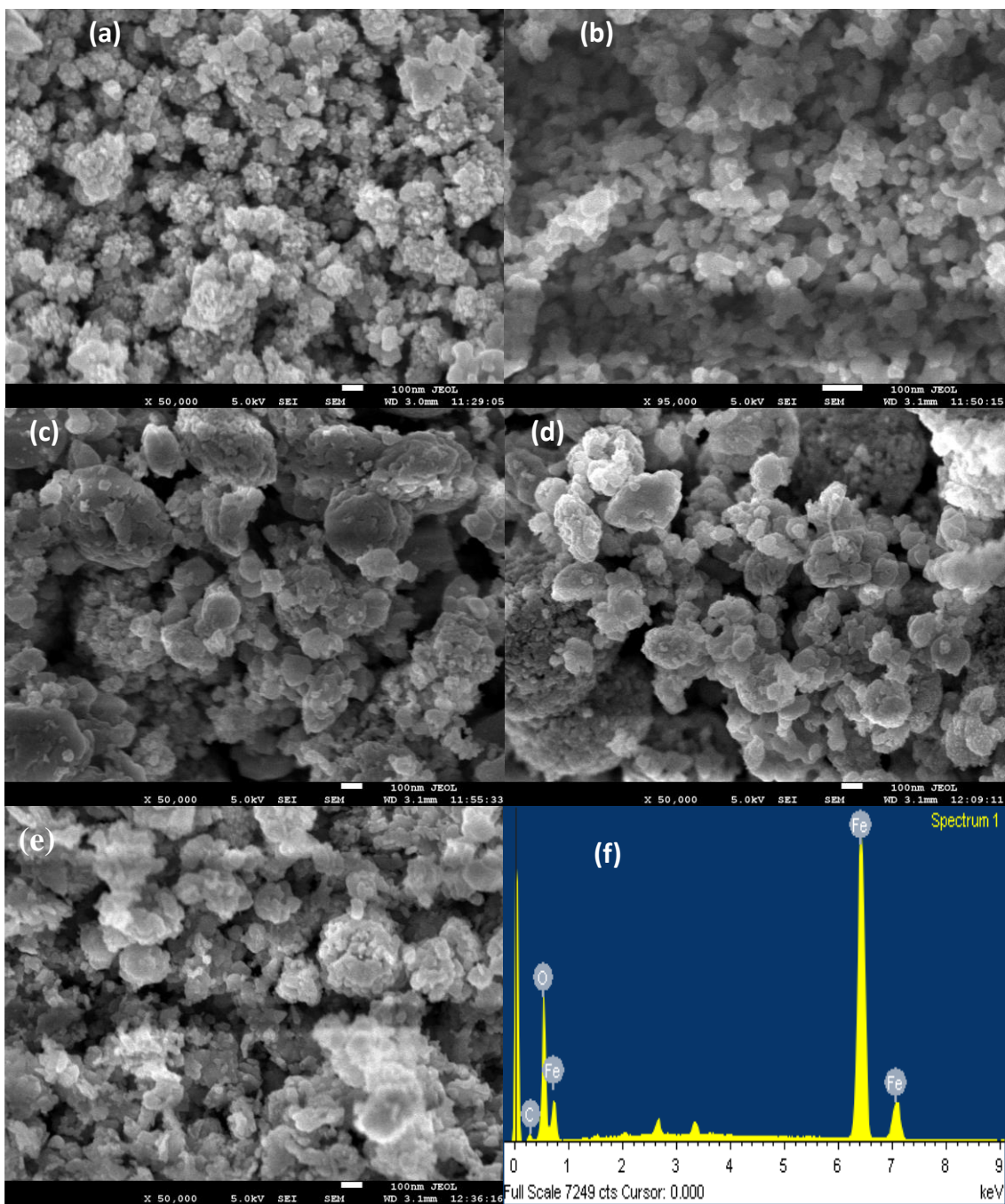


Figure 5. FESEM images of the mesoporous Fe₂O₃ (a) and CNT-Fe₂O₃ nanohybrids at CNT contents 10 wt% (b), 20 wt% (c), 40 wt% (d) and 50 wt% (e); The energy-dispersive spectrum of 50% CNT- α -Fe₂O₃ nanohybrid (f).

Fig. 6 shows TEM images of the mesoporous α -Fe₂O₃ and 20% CNT- α -Fe₂O₃ nanohybrid. TEM image of mesoporous α -Fe₂O₃ could be observed in Fig. 6a. The image exhibited that Fe₂O₃ nanoparticles tend to agglomerate readily, as given in Fig. 6a. The distribution of the nanoparticles size of α -Fe₂O₃ is around 10-30 nm with smooth surfaces (Fig. 6a). Fig. 6c displayed the TEM image of 20% CNT- α -Fe₂O₃ nanohybrid. Fe₂O₃ nanoparticles are well distributed homogeneously in the CNT surface with size <10 nm. Also, the pore size is found to be < 20 nm, which is in conformity with the outcome of BET measurement. The high HRTEM images of the α -Fe₂O₃ and 20% CNT- α -Fe₂O₃ nanohybrid are shown in Figs. 6b,d. They indicated that the regular lattice fringes from α -Fe₂O₃ nanoparticles were obviously visible, with a spacing of 0.252 nm, conforming to the spacing of the (110) planes of α -Fe₂O₃. Selected area electron diffraction (SAED) pattern (Figs. 6b, d inset) further confirm that α -Fe₂O₃ nanocrystallites are formed. Both the pores and small α -Fe₂O₃ nanoparticles are crucial to the photocatalytic performance of CNT- α -Fe₂O₃ nanohybrid as will be addressed hereafter.

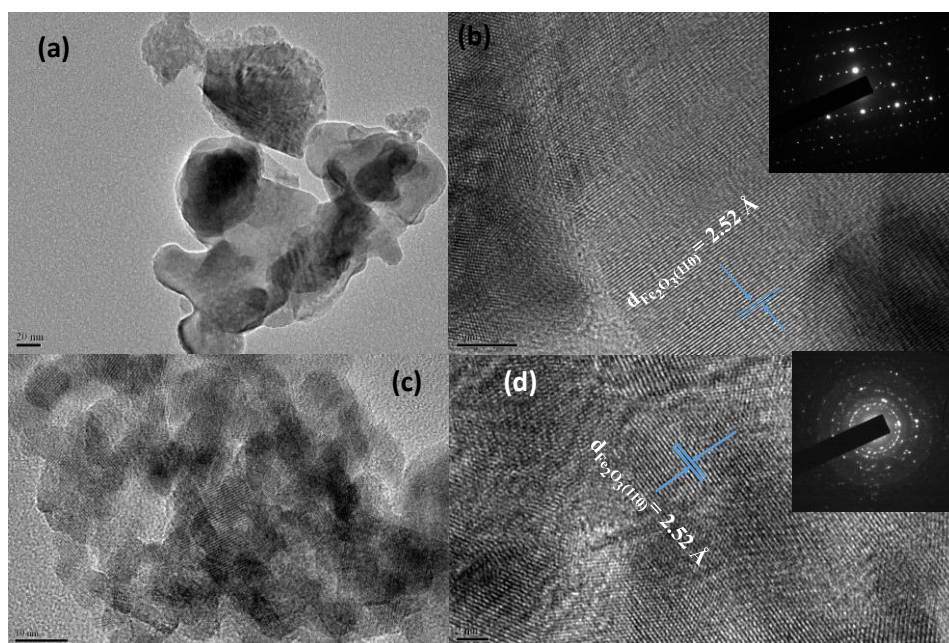


Figure 6. TEM images of mesoporous Fe₂O₃ (a) 20 wt% CNT-Fe₂O₃ nanohybrids(c); HRTEM image of mesoporous Fe₂O₃ (b) 20 wt% CNT-Fe₂O₃ nanohybrids (d), Inset, the SAED pattern of - the mesoporous Fe₂O₃ (b) and 20 wt% CNT-Fe₂O₃ nanohybrids (d).

UV-VIS diffuse reflectance spectra show the of pure Fe₂O₃ and CNT- α -Fe₂O₃ nanohybrids at different CNT contents as depicted in Fig. 7. It can be observed that mesoporous Fe₂O₃ is highly reflective in the visible region. There are slightly change in the absorbance of CNT- α -Fe₂O₃ nanohybrids as a result of changing CNT contents. With the incorporation of CNT into the Fe₂O₃ matrix, the reflection is found to be decreased, i.e. the absorption visible region became wide. The absorbance was shifted to higher wavelength with adding 10% CNT into Fe₂O₃ nanoparticles, however, with increasing CNT more than 10% CNT, the absorbance was reduced to smaller wavelength. The UV-vis data reveal that the

introduction of CNT into Fe_2O_3 up to 50% significantly increased optical band gap from 2.22 to 2.75 eV. The tight band gap energy of the obtained CNT- α - Fe_2O_3 nanohybrids extends the visible region for enhancing optical response and facilitates promotion of photogenerated electron and holes, which is advantageous for their photocatalytic performance upon illumination. The enhanced absorption in the visible region could be explained by the construction of a new dopant energy level beneath the Fe_2O_3 conduction band [36].

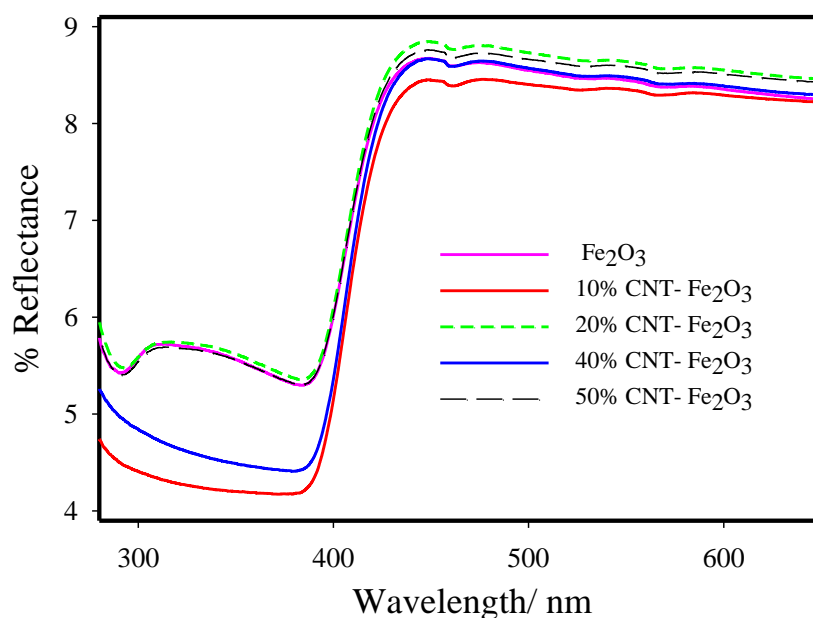


Figure 7. (a) UV-visible diffuse reflectance spectra of the mesoporous Fe_2O_3 and CNT- Fe_2O_3 nanohybrids at different CNT contents 10, 20, 40 and 50 wt%. (b) The plot of transferred Kubelka–Munk against of light absorbed energy of the mesoporous 20 wt% CNT- Fe_2O_3 nanohybrids.

3.2. Adsorption and Photocatalytic investigations of BBR.

We performed a research to determine the potential utility of CNT- α - Fe_2O_3 nanohybrids as a photocatalyst for the decolorization of BBR and total organic carbon (TOC) reduction. The mesoporous CNT- α - Fe_2O_3 nanohybrids dominate superior photocatalytic and adsorption feature than that of pure mesoporous Fe_2O_3 owing to the synergetic effect of mesoporous α - Fe_2O_3 and CNT. Before photocatalytic evaluation, the adsorption performance of BBR over mesoporous α - Fe_2O_3 and CNT- α - Fe_2O_3 nanohybrids at different CNT contents for 60 min in the dark was determined. The results revealed that the BBR adsorption amount is boosted with the increase of retention time. To reach the BBR adsorption equilibrium, 60 min is a good enough time. As for mesoporous CNT- α - Fe_2O_3 nanohybrids, the adsorption amount for BBR is about 85%, which is higher than that of mesoporous Fe_2O_3 ~5%. The adsorption efficiency of 10, 20, 40 and 50 CNT- α - Fe_2O_3 nanohybrids was calculated to be 50, 70, 80 and 85%, respectively (Table 1). One can conclude that the adsorption property of 50% CNT- α - Fe_2O_3 nanohybrids is greater 17 times than that of mesoporous α - Fe_2O_3 . The higher adsorption capacity of the CNT- α - Fe_2O_3 nanohybrids contributes to boosting the photocatalytic efficiency of BBR dye.

To explore the importance of the CNT in the prepared CNT- α -Fe₂O₃ nanohybrids, they were evaluated in the photocatalytic oxidation of BBR dye under visible light. In the photolysis test, the change in the BBR dye concentration after 3 hours is insignificant. The decolorization of BBR dye within 3 hours is 70% by employing the mesoporous α -Fe₂O₃ (Fig. 8 & Table 1). The decolorization of BBR dye gradually increased with the increase of CNT contents (Fig. 8, Table 1). At 50% CNT- α -Fe₂O₃ nanohybrids, the decolorization of BBR dye increased from 70 to reach 95% within 3 h (Fig. 8, Table 1). The CNT- α -Fe₂O₃ nanohybrids were found to be very effective in the decolorization of BBR dye. Thus, CNT- α -Fe₂O₃ nanohybrids showed the practical and potential utility in decolorization of BBR dye. The decolorization rate of BBR dye over CNT- α -Fe₂O₃ nanohybrids at different Fe₂O₃ contents was calculated and outlined in Table 1. The findings revealed that the p decolorization rate of BBR dye was boosted from 1.288×10^{-5} to $4.545 \times 10^{-4} \text{ mol L}^{-1} \text{ s}^{-1}$ with the increase of CNT contents from 0 to 50 wt%. It is evident that the decolorization rate of BBR dye over 50% CNT- α -Fe₂O₃ nanohybrid is nearly 35 times- greater than that of the mesoporous Fe₂O₃ (Table 1). On the other hand, the decrease of the total organic carbon (TOC) with illumination time reflects the mineralization percentage of BBR dye in the solution (Fig. 9, Table 1). The TOC removal throughout BBR dye photooxidation is outlined in Table 1. TOC concentration of BBR dye is 7.1 ppm, decreased to 1.2 ppm after 24 h illumination time, which means the total removal efficiency is 83% with employing mesoporous α -Fe₂O₃. The total removal efficiency was boosted from 83 to 98% with the increase of CNT contents from 0 to 50% (Fig. 9, Table 1). The significant improvement in BBR dye photodegradation can be explained by the synergistic effect among the merging of Fe₂O₃ nanoparticles and CNT [37]. Upon visible light illumination, the Fe₂O₃ nanoparticles acted as good electron donors, while the CNT is playing as electron acceptors.

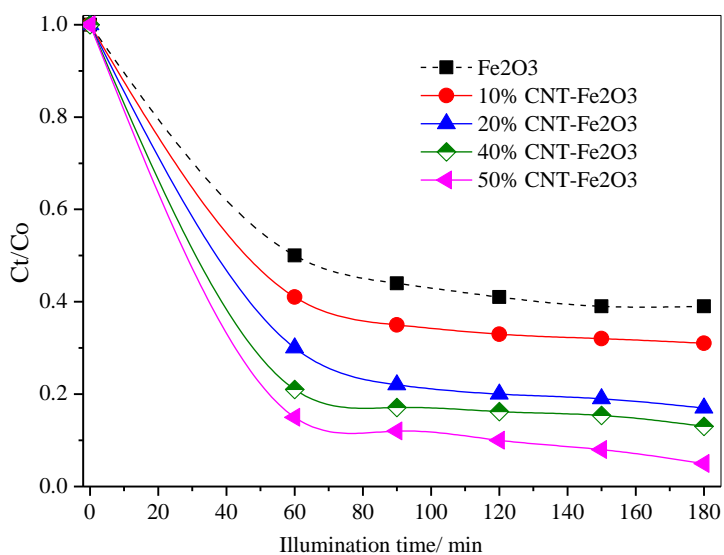


Figure 8. Change in BBR dye absorbance vs. illumination time in the presence of the mesoporous Fe₂O₃ and CNT-Fe₂O₃ nanohybrids at different CNT contents 10, 20, 40 and 50 wt%.

To emphasize the proposed photocatalysis mechanism, the photoluminescence (PL) was utilized to explain the effect of mesoporous Fe₂O₃ and CNT, as well as understanding the bath of e⁻/h⁺ pairs charge carrier trapping. Fig. 10 shows the PL emission spectra of mesoporous α -Fe₂O₃, 20%CNT- α -

Fe_2O_3 , and 50%CNT- α - Fe_2O_3 nanohybrids. Upon excitation at 325 nm wavelength, the mesoporous α - Fe_2O_3 , 20%CNT- α - Fe_2O_3 , and 50%CNT- α - Fe_2O_3 nanohybrid led to strong PL peaks at 467 nm. The emission peak at 467 nm is explained by the charge carriers recombination of the excited Fe_2O_3 surface. The peak was distinctly visible in the excitation spectrum as shown in Fig. 10. An enhancement in PL emission and reduced photoconductivity is observed for 20%CNT- α - Fe_2O_3 and 50%CNT- α - Fe_2O_3 nanohybrid when compared to mesoporous α - Fe_2O_3 . Also, PL emission spectra of mesoporous Fe_2O_3 intensity are higher than that of the CNT- α - Fe_2O_3 nanohybrid (Fig. 10). These findings confirmed that the electron-hole recombination rate of the mesoporous Fe_2O_3 is faster than those CNT- α - Fe_2O_3 nanohybrids. The decline PL intensity of the CNT- α - Fe_2O_3 nanohybrids indicates the increase of the photocatalytic performance [38]. These results are consistent with the photocatalytic efficiency.

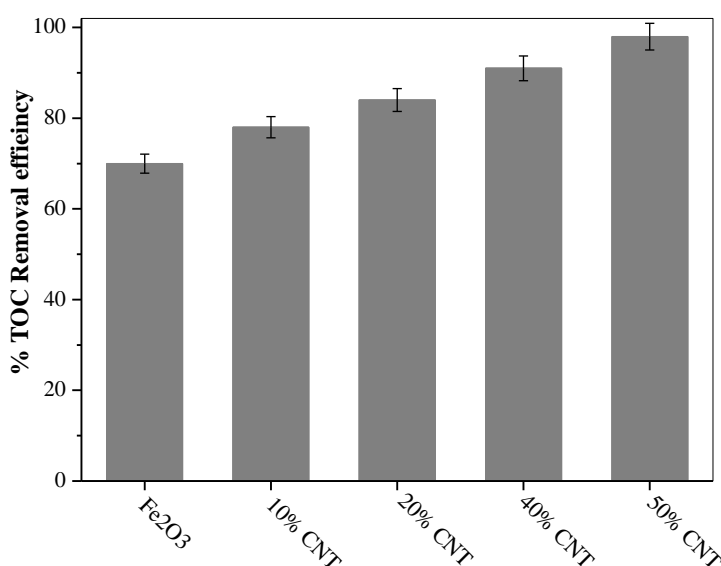


Figure 9. TOC removal efficiency over the mesoporous Fe_2O_3 and CNT- Fe_2O_3 nanohybrids at different CNT contents 10, 20, 40 and 50 wt% for photodegradation of BBR dye.

The reason behind the enhancement of photocatalytic performance of mesoporous Fe_2O_3 after introducing CNT is attributed to the hybridization of mesoporous Fe_2O_3 and CNTs, that could promote the oxidative photodegradation rate, indicating the interfacial electron transport from the Fe_2O_3 nanoparticles to the connected CNT, which suppresses the electrons and holes recombination and hence the enhanced separation of photo-induced electrons and holes. CNT is acting as an electron storage and electrical conductor to collect and transfer the photogenerated electrons delivered from the CB of Fe_2O_3 . Since molecular O_2 is adsorbed onto CNT surface, the photogenerated electrons moved from the CB of Fe_2O_3 to the CNT. They have more chance to reduce the O_2 molecules adsorbed onto CNT, generating O_2^- . Simultaneously, the produced photo-holes on VB of the Fe_2O_3 are taken part in the oxidative species formation and provide the efficient photocatalytic oxidation of BBR dye. Therefore, the recombination of the charge carriers is prohibited, which promotes significantly the photocatalytic performance of the mesoporous Fe_2O_3 under visible light. It is reported that the bandgap of Fe_2O_3 is ~ 2.2 eV and its CB position of Fe_2O_3 is ~ -5.21 eV using vacuum level (AVS) as a reference [39]. The CNT work function

is documented to be 4.3-4.5 eV [40]. When Fe_2O_3 are connected to the CNT surface, the relative CNT conduction band edge position allows the transport of photogenerated electrons from the Fe_2O_3 surface, permitting stabilization, charge carriers separation, and suppressed recombination. The photogenerated electrons can be moved freely along the CNT conducting network. The longer-lived photo-holes on the VB of Fe_2O_3 nanoparticles, then, producing high photocatalytic activity of the mesoporous CNT- α - Fe_2O_3 nanohybrids.

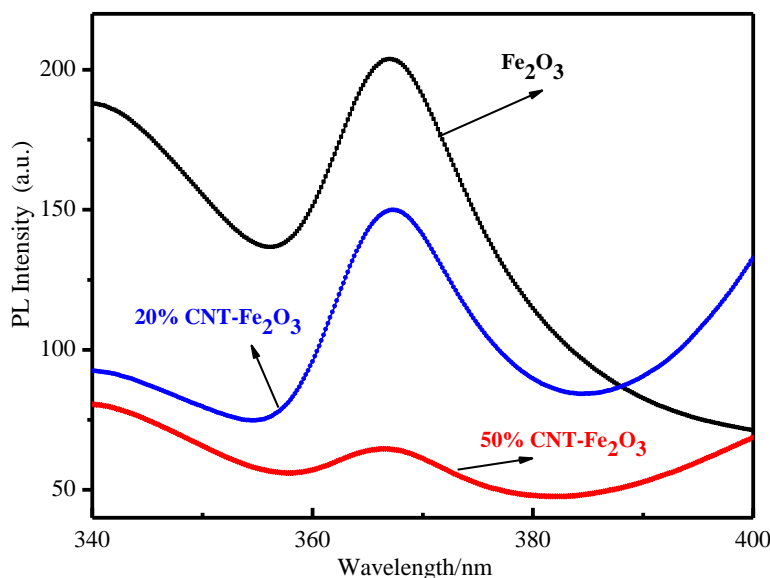


Figure 10. PL spectra of the mesoporous α - Fe_2O_3 , 20%CNT- α - Fe_2O_3 and 50%CNT- α - Fe_2O_3 nanohybrids.

The stability of mesoporous CNT- α - Fe_2O_3 nanohybrids is essentially crucial for the potential application in industrial and domestic wastewater treatment. The stability of the mesoporous 50%CNT- α - Fe_2O_3 nanohybrid was evaluated by 5 times repeating the photooxidation of BBR dye through illumination (Fig. 11). The results of the reusability of the 50%CNT- α - Fe_2O_3 nanohybrid showed that there was no significant decrease in the photocatalytic oxidation of BBR dye and remained above 90%, indicating good photocatalyst stability. Such result reveals that simple washing of CNT- α - Fe_2O_3 nanohybrids is an economical and efficient process for potential practical application.

3.3. Electrochemical Sensing of Phenyl hydrazine using CNT- α - Fe_2O_3 Modified GCE

The electrochemical sensing of phenyl-hydrazine using CNT- α - Fe_2O_3 modified GCE as a sensing working electrode in PBS was smoothly investigated. The fabricated sensor electrode was found to be easy to assemble, electrochemically active and stable upon exposure to air. Fig. 12a shows the current-potential (I - V) response of the applied CNT- α - Fe_2O_3 nanohybrid modified GCE in contact with various concentrations of phenyl-hydrazine (0.01 up to 10 mM) in the presence of 0.1M PBS of pH=7. For better clarity, curves shown in Fig. 12b describe an enlarged section of the I - V response at lower concentrations.

It is a general trend that the measured current increases with the increase of phenyl-hydrazine concentration, essentially due to the increase of the ionic strength of solution [41].

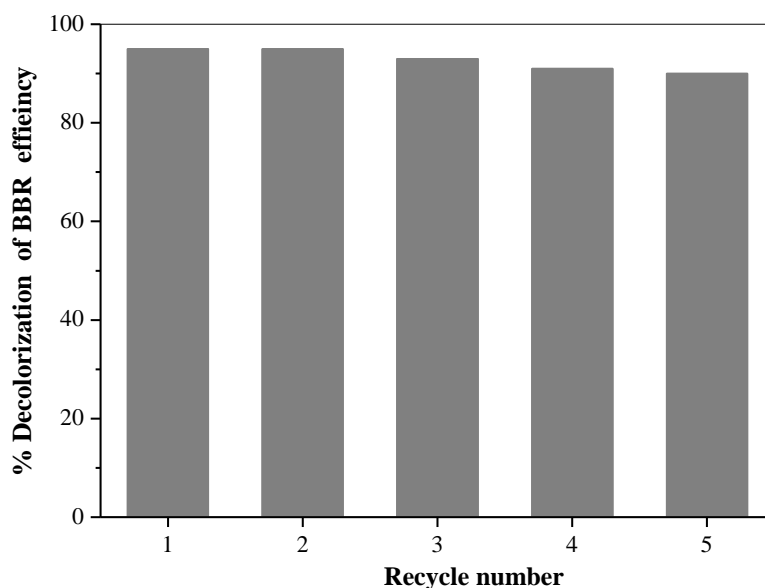


Figure 11. Reusability up to 5 sequences times of photocatalytic oxidation of BBR dye over mesoporous 50% CNT-Fe₂O₃ nano hybrid.

The enhancement of ionic strength would provide more electrons to the conduction band of α -Fe₂O₃, along with the high conductivity of CNT leading together to an observed increase of current response at the modified GCE based sensor [42,43]. Phenyl-hydrazine is known to be converted to diazenyl benzene at specific oxidation potential. Such a conversion process led to release two electrons resulting in the enhancement of the current observed. The involved reactions can be summarized as the following equations [44,45]:



The acting sensing material of CNT- α -Fe₂O₃ likely drives a fast electron exchange and remarkable electrochemical catalytic oxidation behavior toward phenyl-hydrazine. The calibration plot shown in Fig. 12c exhibits a linear relationship over the phenyl-hydrazine concentrations from 10 μ M to 1 mM with ($R^2 = 0.9995$). It is worthy to mention that a deviation from linearity was observed at higher concentrations. From the above calibration plot of the current-concentration profile, the sensor sensitivity can be calculated based on the equation: *sensitivity = slope of calibration plot/electrode surface area*. The sensitivity was accordingly calculated to be 1081 $\mu\text{AmM}^{-1}\text{cm}^{-2}$. At higher concentrations, the sensitivity was found to notably decrease. The linear dynamic concentration range

under the current experimental conditions is from 10 μM up to 1 mM. The limit of detection (LOD) of the current sensor electrode based on; $S/N=3$: signal-to-noise ratio was estimated to be 6.25 μM .

The sensing performance of current modified electrode toward phenyl hydrazine is compared with other sensors in the literature as shown in Table 2 [26,45-47], indicating outstanding sensor response at the current developed electrode, especially for the huge sensitivity and low LOD.

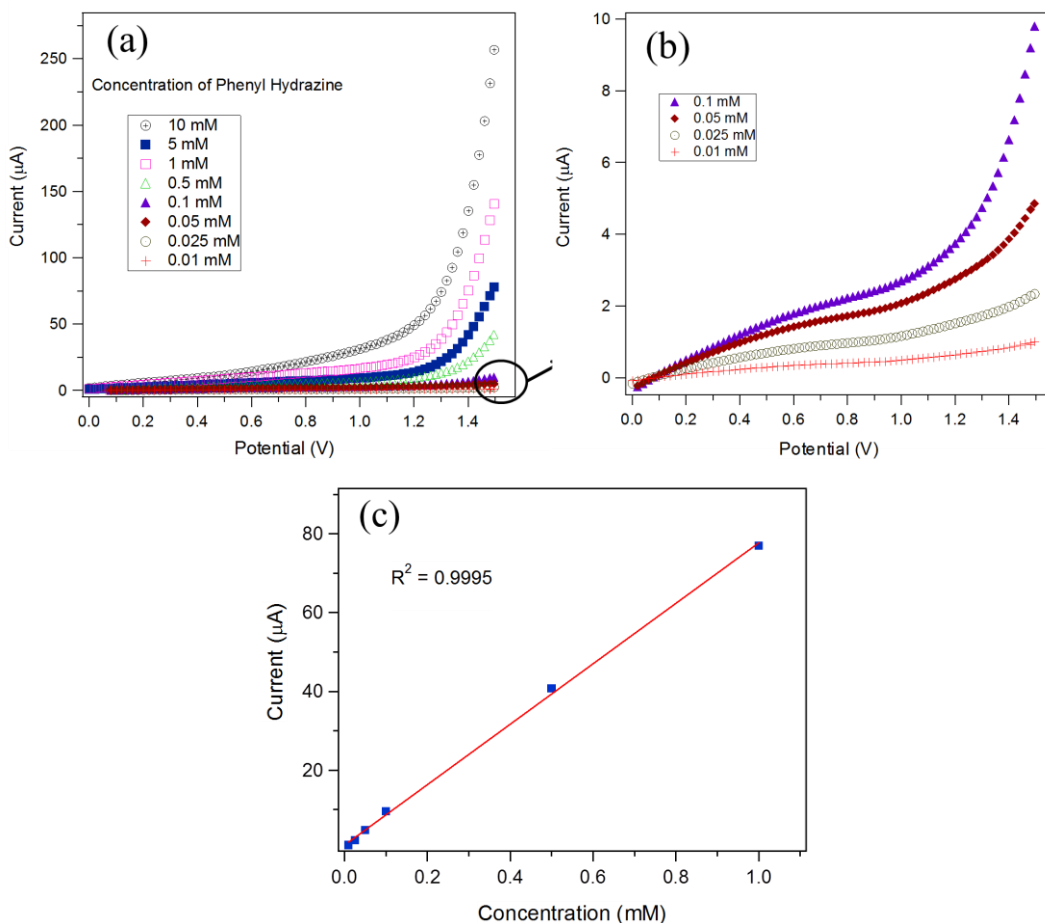


Figure 12. (a) Current-potential (I - V) characteristics of CNT- α - Fe_2O_3 nanohybrid modified GCE in contact with different concentrations of phenyl hydrazine ranging from 0.01 to 10 mM in 0.1 M PBS of pH=7. (b) The enlarged part of the I - V response at lower concentrations. (c) The corresponding calibration plot within the linear range of 0.01 to 1 mM concentration.

Table 2. Comparison between current electrode sensor performance toward phenyl hydrazine and previously reported electrodes using the I - V technique.

Modified electrode	Sensitivity ($\mu\text{AmM}^{-1}\text{cm}^{-2}$)	Linear range (μM -mM)	LOD (μM)	Ref.
Fe_2O_3 NPs	57.88	97-1.56	97	[26]
ZnO- Fe_2O_3	8.33	0.001-10	0.67 nM	[45]
CuO flowers	7.145	5-10	2.4 mM	[46]
ZnO nano-urchin	42.1	98.3.126	78.6	[47]
CNT- α - Fe_2O_3	1081	10-1	6.25	<i>This work</i>

4. CONCLUSIONS

In summary, a facile synthesis to fabricate highly photoactive mesoporous CNT- α -Fe₂O₃ nanohybrids at different CNT contents has been demonstrated. They exhibited outstanding photocatalytic performance under visible light owing to enhance charge carrier separation. The optimized mesoporous 50%CNT- α -Fe₂O₃ nanohybrid indicated the highest photocatalytic efficiency compared with mesoporous α -Fe₂O₃. The photocatalytic performance of mesoporous CNT- α -Fe₂O₃ nanohybrids for photocatalytic oxidation of BBR dye indicates that this nanohybrid is a favorable candidate as photocatalyst and absorbent for industrial and domestic wastewater treatment. The enhancement of photocatalytic activity of CNT- α -Fe₂O₃ nanohybrids is explained by the synergistic effect between Fe₂O₃ nanoparticles and CNT. A synergistic effect has remarkably enhanced the photocatalytic degradation efficiency of BBR in comparison with that pure mesoporous Fe₂O₃. The photocatalyst was recycled five times very efficiently with slight loss in the photocatalytic performance. Furthermore, the developed CNT- α -Fe₂O₃ nanohybrid was used as active sensing material onto glassy carbon electrode for the detection of phenyl hydrazine in aqueous solutions over the concentration range of 10 μ M up to 1.0 mM, giving outstanding sensitivity 1081 μ AmM⁻¹cm⁻² and low limit of detection 6.25 μ M.

ACKNOWLEDGEMENTS

The authors extend their appreciation to the Deanship of Scientific Research at King Khalid University, Abha, Kingdom of Saudi Arabia for funding this work through General Research Project under grant number G.R.P-80-38.

References

1. J. Zhu, J. Jiang, J. Liu, R. Ding, Y. Li, H. Ding, Y. Feng, G. Wei, X. Huang, *RSC Adv.*, 1 (2011) 1020.
2. R. Leary, *Carbon*, 49 (2011) 741.
3. L.M. Ang, T.S.A. Hor, G.Q. Xu, C.H. Tung, S. P. Zhao, J.L.S. Wang, *Carbon*, 38 (2000) 363.
4. M. J. Ledoux, R. Vieira, C. Pham-Huu, N. Keller, *J. Catal.*, 216 (2003) 333.
5. X. Sun, B. Stansfield, J. P. Dodelet, S. Désilets, *Chem. Phys. Lett.*, 363 (2002) 415.
6. E.A. Whitsitt, A.R. Barron, *Nano Lett.*, 3 (2003) 775.
7. W.Q. Han, A. Zettl, *Nano Lett.*, 3 (2003) 681.
8. J. Sun, L. Gao, W. Li, *Chem. Mater.*, 14 (2002) 5169.
9. J. Sun, L. Gao, *Carbon*, 41 (2003) 1063.
10. S. M. El-Sheikh, G. Zhang, H. M. El-Hosainy, A. A. Ismail, K. O'Shea, P. Falaras, A. G. Kontos, D. D. Dionysiou, *J. Hazard. Mater.*, 280 (2014) 723.
11. B.-Y. Wei, M-C. Hsu, P-G. Su, H-M. Lin, R-J. Wu, H-J. Lai, *Sens. Actuators B*, 101 (2004) 81.
12. F. Vietmeyer, B. Seger, P.V. Kamat, *Adv. Mater.*, 19 (2007) 2935.
13. X. Xie, L. Gao, *Carbon*, 45 (2007) 2365.
14. J.H. Park, J.M. Ko, O.O. Parka, *J. Electrochem. Soc.*, 150 (2003) A864.
15. P.G. Bruce, *Solid State Sci.*, 7 (2005) 1456.
16. J.B. Fei, Y. Cui, X. H. Yan, W. Qi, J. B. Li, *Adv. Mater.*, 20 (2008) 452.
17. J. Chen, L. Xu, W.Y. Li, X.L. Gou, *Adv. Mater.*, 17 (2005) 582.
18. C. Guo, H. Li, X. Zhang, H. Huo and C. Xu, *Sens. Actuators*, 206 (2015) 407.
19. J.W. Long, M.S. Logan, C.P. Rhodes, E.E. Carpenter, D.R. Rolison, *Am. Chem. Soc.*, 126 (2004)

- 16879.
20. F. Jiao, P.G. Bruce, *Angew. Chem.*, Two- and three-dimensional mesoporous iron oxides with microporous walls, *Int. Ed.* 43 (2004) 5958.
 21. A.G. Kong, H.W. Wang, J. Li, Y.K. Shan, *Mater. Lett.*, 62 (2008) 943.
 22. C.T. Kresge, M.E. Leonowicz, W. J. Roth, J.C. Vartuli, J.S. Beck, *Nature*, 359 (1992) 710.
 23. S.M. El-Sheikh, T.M. Khedr, A. Hakki, A.A. Ismail, W.A. Badawy, D.W. Bahnemann, *Separation and Purification Technology*, 173 (2017) 258.
 24. A.A. Ismail, D.W. Bahnemann, L. Robben, M. Wark, *Chem. Mater.*, 22 (2010) 108.
 25. A.A. Ismail, D.W. Bahnemann, *J. Phys. Chem. C*, 115 (2011) 5784-5791.
 26. S.W. Hwang, A. Umar, G.N. Dar, S.H. Kim, R.I. Badran, *Sensor Lett.* 12 (2014) 97-101.
 27. H.B. Zhang, G.D. Lin, Z.H. Zhou, X. Dong, T. Chen, *Carbon*, 40 (2002) 2429.
 28. L. Chen, X. Yang, J. Chen, J. Liu, H. Wu, H. Zhan, C. Liang, M. Wu, *Inorg. Chem.*, 49 (2010) 8411.
 29. V.V. Bolotov, V.E. Kan, E.V. Knyazev, P.M. Korusenko, S.N. Nesov, Y.A. Stenkin, V.A. Sachkov, I.V. Ponomareva, *New Carbon Mater.*, 30 (2015) 385.
 30. C.-S. Chen, T.-G. Liu, X.-H. Chen, L.-W. Lin, Q.-C. Liu, Q.-Xia, Z.-W. Ning, *Trans. Nonferr. Met. Soc. China*, 19 (2009) 1567.
 31. M. Morsy, M. Helal, M. El-Okri, M. Ibrahim, *Spectrochim. Acta A*, 132 (2014) 594.
 32. I.T. Kim, G.A. Nunnery, K. Jacob, J. Schwartz, X. Liu, R. Tannenbaum. *J. Phys. Chem. C*, 114 (2010) 6944.
 33. A. Millan, F. Palacio, A. Falqui, E. Snoeck, V. Serin, A. Bhattacharjee, V. Ksenofontov, P. Gutlich, I. Gilbert, *Acta Mater.*, 55 (2007) 2201.
 34. Y. Yang, T. Liu, *Appl. Surf. Sci.*, 257 (2011) 8950.
 35. S.J. Gregg, K.S.W. Sing, *Adsorption, surface area and porosity*, Academic Press: London, 1982.
 36. X. Liu, M.K. Devaraju, S. Yin, A. Sumiyoshi, T. Kumei, K. Nishimoto, T. Sato, *Dyes and Pigments*, 84 (2010) 237.
 37. K.H. Ji, D.M. Jang, Y.J. Cho, H.S. Kim, Y. Kim, J. Park, *J. Phys. Chem. C*, 113 (2009) 19966.
 38. A.A. Ismail, I. Abdelfattah, M. Faisal, A. Helal, *J. Hazardous Mater.*, 342 (2018) 519.
 39. Y. Xu, M.A.A. Schoonen, The absolute energy positions of conduction and valence bands of selected semiconducting minerals'. *In: American Mineralogist*, 85 (2000) 543.
 40. A. Sherehiy, S. Dumpala, A. Safir, D. Mudd, I. Arnold, R.W. Cohn, M.K. Sunkara, G.U. Sumanasekera, *Diamond & Related Materials*, 34 (2013) 1.
 41. O. Akhavan, E. Ghaderia, *J. Mater. Chem.*, 21 (2011) 12935.
 42. C. Yuan, Y. Xu, Y. Deng, N. Jiang, N. He, L. Dai, *Nanotechnology*, 21 (2010) 415501.
 43. F.A. Harraz, A.A. Ismail, A.A. Ibrahim, S.A. Al-Sayari, M.S. Al-Assiri, *Chem. Phys. Lett.*, 639 (2015) 238.
 44. A.M. Ali, F.A. Harraz, A.A. Ismail, S.A. Al-Sayari, H. Algarni, A.G. Al-Sehemi, *Thin Solid Films*, 605 (2016) 277.
 45. M.M. Rahman, G. Gruner, M.S.d Al-Ghamdi, M.A. Daous, S.B. Khan, A.M. Asiri, *Int. J. Electrochem. Sci.*, 8 (2013) 520.
 46. S.B. Khan, M. Faisal, M.M. Rahman, I.A. Abdel-Latif, A.A. Ismail, K. Akhtar, A. Al-Hajry, A.M. Asiri, K.A. Alamry, *New J. Chem.*, 37 (2013) 1098.
 47. A. Umar, M.S. Akhtar, A. Al-Hajry, M.S. Al-Assiri, G.N. Dar, M.S. Islam, *New J. Chem.*, 37 (2013) 1098.